Video Article

Photoelectron Imaging of Anions Illustrated by 310 Nm Detachment of F^-

Justin Lyle[1], Sudharson Ravishankar Chandramoulee[1], C. Annie Hart[1], Richard Mabbs[1]

[1]Department of Chemistry, Washington University in St. Louis

Correspondence to: Richard Mabbs at mabbs@wustl.edu

URL: https://www.jove.com/video/57989
DOI: doi:10.3791/57989

Keywords: Chemistry, Issue 137, Chemical physics, physical chemistry, photoelectron spectroscopy, gas phase anions, velocity mapped imaging, electronic structure

Date Published: 7/27/2018

Citation: Lyle, J., Chandramoulee, S.R., Hart, C.A., Mabbs, R. Photoelectron Imaging of Anions Illustrated by 310 Nm Detachment of F^-. *J. Vis. Exp.* (137), e57989, doi:10.3791/57989 (2018).

Abstract

Anion photoelectron imaging is a very efficient method for the study of energy states of bound negative ions, neutral species and interactions of unbound electrons with neutral molecules/atoms. State-of-the-art in vacuo anion generation techniques allow application to a broad range of atomic, molecular, and cluster anion systems. These are separated and selected using time-of-flight mass spectrometry. Electrons are removed by linearly polarized photons (photo detachment) using table-top laser sources which provide ready access to excitation energies from the infra-red to the near ultraviolet. Detecting the photoelectrons with a velocity mapped imaging lens and position sensitive detector means that, in principle, every photoelectron reaches the detector and the detection efficiency is uniform for all kinetic energies. Photoelectron spectra extracted from the images via mathematical reconstruction using an inverse Abel transformation reveal details of the anion internal energy state distribution and the resultant neutral energy states. At low electron kinetic energy, typical resolution is sufficient to reveal energy level differences on the order of a few millielectron-volts, *i.e.*, different vibrational levels for molecular species or spin-orbit splitting in atoms. Photoelectron angular distributions extracted from the inverse Abel transformation represent the signatures of the bound electron orbital, allowing more detailed probing of electronic structure. The spectra and angular distributions also encode details of the interactions between the outgoing electron and the residual neutral species subsequent to excitation. The technique is illustrated by the application to an atomic anion (F^-), but it can also be applied to the measurement of molecular anion spectroscopy, the study of low lying anion resonances (as an alternative to scattering experiments) and femtosecond (fs) time resolved studies of the dynamic evolution of anions.

Video Link

The video component of this article can be found at https://www.jove.com/video/57989/

Introduction

Anion photoelectron imaging[1] is a variant on photoelectron spectroscopy and represents a powerful probe of atomic/molecular electronic structure and the interactions between electrons and neutral species. The information obtained is essential in developing the understanding of bound and metastable (electron-molecule scattering resonances) negative ion states, doorway states for chemical reduction, dissociative attachment processes and ion-molecule interactions. Furthermore, the results provide vital tests of high level *ab initio* theoretical methods, particularly those designed to deal with highly correlated systems and/or non-stationary states.

The technique combines ion production, mass spectrometry and charged particle imaging[2,3,4] to sensitively probe electronic (and for small molecules, vibrational) structure. Working with anionic species allows good mass selectivity via time of flight mass spectrometry (TOF-MS). Visible/near ultraviolet (UV) photons are sufficiently energetic to remove the excess electron, allowing the use of table top laser sources. An additional benefit of the use of anions is the ability to photoexcite low-lying, unstable anionic states which represent energy regimes under which the electrons and neutral atoms/molecules strongly interact. The use of velocity mapped imaging[5] (VMI) affords uniform detection efficiency, even at low electron kinetic energies, monitors all ejected photoelectrons and simultaneously reveals the magnitude and direction of their velocities.

The experimental results are photoelectron images which contain photoelectron spectra (details of parent anion internal energy distributions and the energies of daughter neutral internal states) and photoelectron angular distributions (related to the electron orbital prior to the detachment). A particularly interesting application of the technique is found in fs time-resolved studies. An initial ultrafast laser pulse (pump) excites to a dissociative anion electronic state, and a second temporally delayed ultrafast pulse (probe) then detaches electrons from the excited anion. The control of the pump-probe time difference follows the evolution of energy states of the system and the changing nature of the orbitals of the system on the timescale of the atomic motion. Examples include the photodissociation of I_2^- and other interhalogen species[6,7,8,9], the fragmentation and/or electron accommodation in I^-·uracil[10,11,12,13], I^-·thymine[13,14], I^-·adenine[15], I^-·nitromethane[16,17] and I^-·acetonitrile[17] cluster anions and the revelation of the hitherto unexpectedly long timescale for the production of Cu^- atomic anions after the photoexcitation of CuO_2^-[18].

Figure 1 shows the Washington University in St. Louis (WUSTL) anion photoelectron imaging spectrometer[19]. The instrument consists of three differentially pumped regions. Ions are produced in the source chamber which operates at a pressure of 10^{-5} Torr and contains a discharge ion source[20], and electrostatic ion extraction plate. Ions are separated by mass in a Wiley-McLaren TOF-MS[21] (the pressure in the TOF-Tube is 10^{-8} Torr). Ion detection and probing takes place in the detection region (pressure of 10^{-9} Torr) which contains a VMI lens[5] and a charged particle detector. The main components of the instrument are schematically illustrated in **Figure 1b** where the shaded region represents all the elements contained within the vacuum system. Gas is introduced through the pulsed nozzle into the discharge. To offset the high inlet pressure, the source chamber is maintained under vacuum using an oil-based diffusion pump. The discharge region is illustrated in more detail in **Figure 2a**. A high potential difference is applied between the electrodes, which are insulated from the face of the nozzle by a series of Teflon spacers. In fact, the Teflon acts as the source of fluorine atoms for the results shown later.

The discharge produces a mixture of anions, cations and neutral species. The ion extraction plate, ion acceleration stack, potential switch and microchannel plate (MCP) detector (**Figure 1b**) form the 2 m long Wiley McLaren TOF-MS. Ions are extracted by the application of a (negative) voltage pulse to the ion extraction plate and then all ions are accelerated to the same kinetic energy. Variation of the extraction pulse magnitude focuses the arrival time in the VMI lens while the einzel lens reduces the spatial cross section of the ion beam. Anions are re-referenced to ground using a potential switch[22], the timing of which acts as a mass discriminator. Anion selection is achieved by synchronizing the arrival of a visible/near uv photon pulse with the arrival time of the anion in the VMI lens. The ion separation and detection regions use oil free turbopumps to protect the imaging detector.

Anions and photons interact to produce photoelectrons throughout the spatial volume of the Steinmetz solid, representing the overlap between the ion and laser beams. The VMI lens (**Figure 2b**) consists of three open electrodes, the purpose of which is to ensure that all photoelectrons reach the detector and that the momentum space distribution of the photoelectrons is maintained. To achieve this, different voltages are applied to the extractor and repeller such that, regardless of the spatial point of origin, electrons with the same initial velocity vector are detected at the same point on the detector. The detector consists of a set of chevron-matched MCPs which act as electron multipliers. Each channel has a diameter on the order of a few microns, localizing the gain and preserving the initial impact position. A phosphor screen behind the MCPs indicates the position via the amplified electron pulse as a flash of light which is recorded using a charge coupled device (CCD) camera.

The timing and duration of the various voltage pulses required are controlled using a pair of digital delay generators (DDG, **Figure 3**). The whole experiment is repeated on a shot by shot basis with a repetition rate of 10 Hz. For each shot, several ions and photons interact producing a few detection events per camera frame. Several thousand frames are accumulated into an image. The image center represents the momentum space origin and hence the distance from the center (r) is proportional to the speed of an electron. Angle θ, (relative to the photon polarization direction) represents the direction of an electron's velocity. An image contains the distribution of detection event densities. Thus, it can also be viewed as representing the probability density for detection (at a given point) of an electron. Invoking the Born interpretation of the wave function (ψ) an image represents $|\psi|^2$ for the photoelectron[23].

The 3D electron probability density is cylindrically symmetric about the polarization of the electric vector ($\boldsymbol{\varepsilon}_p$) of the radiation with consequent scrambling of information. Reconstruction of the original distribution is achieved mathematically[24,25,26,27]. The radial distribution (of electrons) in the reconstruction is the momentum (velocity) domain photoelectron spectrum which is converted into the energy domain via application of the appropriate Jacobian transformation.

The anion photoelectron imaging spectrometer (**Figure 1**) used in these experiments is a custom-built instrument[28]. The settings in **Table 1** and **Table 2** for the protocol are specific to this instrument for the production of F^- and imaging of its photoelectron distribution. Several similar versions of the design are used in various research laboratories[6,29,30,31,32,33,34,35,36,37,38,39,40,41,42], but no two instruments are exactly alike. Additionally, instrument settings are strongly interdependent and highly sensitive to small changes in conditions and instrument dimensions.

Protocol

NOTE: A general experimental protocol is presented here, specific to the WUSTL instrument. Specific instrument settings for the F^- image presented in **Figure 4a** can be found in **Table 1-2**.

1. Ion Generation

1. To generate anions, apply a backing gas or gas mixture (for F^-, 40 psig. of O_2) behind the pulsed nozzle and operate the nozzle at 10 Hz.
    1. Set the nozzle duration on digital delay generator 1 (DDG1), channel A (A1) and trigger the pulsed nozzle driver to inject the gas into discharge.
    2. Apply a high voltage discharge pulse V1. The timing and duration of the pulse are controlled by channel C (C1) on DDG1.
    3. As the escape of O_2 gas can lead to increased laboratory fire risk, ensure that all gas lines are leak tight. Since high gas pressures can lead to failure of gas lines, ensure that the pressure is kept below maximum operating pressure. Ensure that power supplies are properly grounded and switched off when cables are being attached or removed.

2. Ion Extraction, Separation and Detection

1. To extract anions from the source, apply a high voltage extraction pulse (V2) to the ion extraction plate.
    1. Set the timing and duration of the ion extraction pulse using DDG1 channel D (D1).

2. To monitor the anion mass spectrum, put the instrument into ion mode.
    1. Connect the detector voltage divider to the imaging detector MCPs.
    2. Apply voltage V11 to the detector anode (phosphor screen).
    3. Connect the ion detector voltage divider output to the oscilloscope channel 1 input.

4. Connect the MCP power supply to the voltage divider input and gradually increase voltage. An input voltage V9 provides V7 to the entry side and V8 to the exit side of the MCP.
   CAUTION: Do not exceed maximum allowable voltage for MCPs.

3. Separate the anions by TOF-MS.
   1. Set the acceleration stack voltage V3.
   2. Using DDG1 channel E (E1), set the timing and duration for the potential switch high voltage pulse (V3).
   3. Externally trigger the oscilloscope from DDG1 channel F (F1) to set the TOF-MS time scale.

4. Adjust the discharge and extraction pulse magnitudes (V1-V2), discharge, extraction, potential switch and nozzle timing and duration through channels A-E on DDG1 to produce ion signal on the oscilloscope.

3. Ion Yield and Resolution Optimization.

NOTE: Steps 3.1 and 3.2 should be repeated iteratively to obtain the optimum resolution and ion yield. (**Tables 1-2** show the settings used to generate the F^- image shown in the results section).

1. To optimize the number of anions of a given species, adjust the ion source settings.
   1. Adjust the pressure of O_2 gas behind the nozzle using the regulator on the gas cylinder.
   2. Adjust the pulsed nozzle duration of operation (A1).
   3. Adjust the magnitude of the discharge pulse voltage (V1).
   4. Adjust the timing and duration of the discharge pulse voltage (C1).
   5. Adjust the timing and duration of the ion extraction pulse (D1).
   6. Adjust the duration the potential switch is at high voltage (E1).
   7. Adjust the voltage on central element of the einzel lens (V4). The ion peaks on the oscilloscope should increase in intensity.
      CAUTION: Ensure O_2 pressure is kept below maximum operating pressure.

2. Adjust the TOF-MS settings to optimize the mass spectral resolution and ion separation
   1. Adjust the ion extraction voltage (V2) to achieve Wiley-McLaren focusing. The ion peaks on the oscilloscope should narrow.
   2. Adjust the acceleration stack voltage V3.

4. Photoelectron Production and Detection

1. Switch the spectrometer to the imaging mode.
   1. Reduce the voltage applied to the ion detector voltage divider (V9) to zero.
   2. Disconnect the ion detector voltage divider from the MCPs.
   3. Connect the MCP and imaging power supplies to the imaging high voltage pulse.
   4. Connect the imaging high voltage pulse to the imaging MCPs

2. Apply a permanent voltage to phosphor screen (V11) and MCPs (V9).
3. Synchronize the arrival time of laser pulses from the nanosecond (ns) dye laser with the arrival time of the ion of interest within the VMI lens.
   1. Connect the fast photodiode to oscilloscope channel 2.
   2. Externally trigger the Nd:YAG laser flash lamps and Q switch using DDG2 channels H (H2) and G (G2). Adjust the timing of the laser trigger (H2) until the photodiode output is close to but preceding the ion signal of interest.
   3. Apply voltage to the imaging repeller (V5) and extractor (V6) electrodes.
   4. Set the camera to long exposure and adjust the laser trigger timing (H2) to maximize the number of electron detection events observed on the PC screen.
      CAUTION: Class IV laser radiation will permanently damage eyesight. Wear appropriate eye protection. Do not look directly into the beam even when wearing eye protection. Avoid specular reflections.

4. Apply a high voltage pulse to the MCP timed to coincide with arrival of the photon pulse to amplify electron signal within the photoelectron production window.
   1. Set the imaging pulse voltage (V10).
   2. Set the imaging pulse timing and duration using DDG2 channel F (F2) such that the imaging pulse is centered on the arrival time of the photon pulse.

5. Image Focusing

1. Set the camera to short exposure.
   1. Trigger the CCD camera to open at the start of an experimental cycle using DDG2 channel E (E2).

2. Collect a background-subtracted image
   1. Collect several frames with the laser pulse coincident with the anion of interest.
   2. Collect several frames with the laser pulse not coincident with any anion.
   3. Subtract the frames collected off coincidence from the frames collected on coincidence.
   4. Repeat step 5.2 and accumulate an image.

3. Adjust the imaging repeller (V5) and extraction (V6) electrode voltages. Generate a new image by repeating step 5.2. The best focusing condition is achieved when the image features are at their narrowest.

6. Image Collection

1. With the camera in short exposure mode, switch to centroided collection.
2. Repeat step 5.2 at the optimum focusing condition to accumulate a sub-pixel resolution image.

7. Data Extraction

NOTE: The data manipulations performed in this section are performed using specifically written programs in the MatLab platform.

1. Locate the center of the image by determining the center of mass (intensity) of the image, using the inherent symmetry of the image to find the center of inversion, or (in the case of low signal to noise) iteratively minimizing the width of the transitions in the spectrum by selecting different trial centers.
    1. Inverse Abel transform the image to recover the 3D velocity distribution.

2. Generate photoelectron spectra
    1. Integrate the intensity as a function of angle for all radii (this is the spectrum in the radial and hence momentum or velocity domain). In practice this is acheived by summation over all radii.
    $$I(r) = \sum_{\theta=0}^{2\pi} I(r,\theta)$$
    where I(r) is the radial intensity and I(r,θ) is the intensity at point r, θ.
    2. Calibrate the spectrum for electron kinetic energy by comparison with an image recorded under the same conditions with transitions of known eBE.
    eKE = eKEcal×$(r/r_{cal})^2$
    where eKE_{ref} is the kinetic energy of a known transition in the reference spectrum, r_{ref} is the radius of the ring in the reference image corresponding to this transition and eKE is the kinetic energy associated with radius r in the experimental image.
    3. Convert the radial spectrum to the energy domain via Jacobian transformation. The energy corresponding to a given r is determined as in 7.2.2. The intensity I(r) is divided by √eKE.

3. Angular Distribution of electrons.
    1. Select a transition in the spectrum.
    2. For different small angular ranges, integrate over the radial range associated with the transition and plot against θ. In practice the integration is acheived by summation over all radii in the range r_0 -FWHM/2 to +FWHM/2.
    $$I(\theta) = \sum_{r0-FWHM/2}^{r0+FWHM/2} I(r,\theta)$$
    where I(θ) is the angular intensity, r0 is the radial value of the transition maximum and FWHM is the full width at half maximum across the radial range of the transition.

Representative Results

By centroiding[43] the data recorded on the 640×480 pixel CCD array of the camera, a grid resolution of 6400×4800 is possible. However, extraction of the spectra and angular distributions involves inverse Abel transformation of the data which requires the image intensity to vary relatively smoothly. As a compromise, the centroided data is "binned" by summing n×n blocks of points. Similar treatment is also necessary for the display of imaging results.

The displayed image and reconstruction of **Figure 4a** is the result of photodetachment from F^- at a photon energy of 4.00 eV (310 nm). The cylindrical symmetry of the photoelectron distribution means that each experimental image contains four equivalent measurements of a momentum space point. **Figure 4a** shows the left half of the experimentally measured image, binned to n = 8, while the right half of **Figure 4a** is an inverse Abel transformation of the data displayed at the same resolution. The image is comprised of a total of 50,000 frames recorded with the laser in coincidence with the F^- ions and an equal number of background frames subtracted. The direction of the laser electric vector ($\boldsymbol{\varepsilon_p}$) is vertical in the plane of the image, as indicated by the double headed arrow.

The image shows two concentric circles. These correspond to the two narrow transitions seen in the photoelectron spectrum. This is extracted from the centroided data binned to n = 4, after inverse Abel transformation, by integrating intensity over all angles (θ) for each radial distance (r) from the center. The r to electron kinetic energy (eKE) scale conversion is affected by calibration with a transition of known kinetic energy (eKE_{cal}) where r_{cal} is the radial distance to the center of the calibration transition.

$$eKE = \left(\frac{r}{r_{cal}}\right)^2 eKE_{cal}$$

The intensities are scaled by the appropriate Jacobian transformation to yield the spectrum shown in **Figure 4b**. The intensity scale has been further adjusted to show the intensities relative to the strongest of the transitions.

The two transitions reflect the existence of two low lying electronic states of neutral F. Labelling according to their electronic angular momenta, these are termed $^2P_{3/2}$ and $^2P_{1/2}$. The two F atom states originate from the $1s^22s^22p^5$ electron configuration. In simple language, the two states differ in the spin of the unpaired electron. The strength of the interaction between spin and orbital angular momenta is different in either case. The electron kinetic energies are dependent on the photon energy (*hv*) and the energy required to produce the final neutral state (the electron binding energy, eBE). These properties are linked by conservation of energy, *eKE* = *hv* - *eBE*. Thus, the highest eKE transition (0.598 eV) represents the lowest binding energy (3.402 eV), which is the electron affinity of a fluorine atom[44]. The difference in the transition kinetic energies (0.598 eV − 0.548 eV) shows that the first excited state of the F atom is just 50 meV higher in energy than the ground state, a measure of the strength of the spin-orbit interaction. The relative strengths of the two transitions (2:1 ratio) reflects the degeneracies of the two F atom electronic states.

The distribution of electrons in the image of **Figure 4a** is not uniform for a given transition. This is shown more quantitatively in **Figure 4c**. The plot shows that for each transition ($\rightarrow^2P_{3/2}$, red open circles, $\rightarrow^2P_{1/2}$, blue filled circles) the electron intensity is greatest at θ = 90° and therefore there is a preference for electrons to be ejected perpendicular to $\boldsymbol{\varepsilon_p}$. This is expected (based on arguments involving angular momentum conservation) for electron removal from a *p* orbital, and the results would be quite different if the electrons were detached from an s orbital[45,46]. The angular distributions are diagnostic of the spatial part of a particular parent orbital. If the data of **Figure 4c** are rescaled (relative to the angular maxima for the respective transitions) as shown in **Figure 4d**, it can be seen that within the limits of the experimental noise, the distributions are almost identical.

The velocity resolution achieved is strongly influenced by the design and details of the experiment. Regarding velocity mapping, the spatial volume within which the electrons are produced, the location of this volume within the imaging lens and the voltages applied to the imaging electrodes are all critical. For the best resolution the volume represented by the intersection of the anion and laser beams should be minimized. In practice this is achieved by reducing the width of the laser and ion beams, either by collimation or focusing. The velocity mapping is very sensitive to the imaging electrode voltages. The image of **Figure 5a** represents the optimal focusing condition, a ratio of 0.700 between repeller and extractor. Even small alterations to this ratio (by changing the repeller or extractor electrode voltages) are detrimental to the velocity resolution. **Figure 5b** shows an image obtained after reducing the ratio to 0.686 (*i.e.*, by little more than 3%). It is clear in both the image and the accompanying spectrum that it is no longer possible to distinguish the two transitions in the spectrum. In fact, the precision of the power supplies to the imaging electrodes places a limit in the effectiveness of the mapping.

Images should display four-way symmetry. In any experiment the probabilistic nature of electron detection will always lead to small deviations from this expectation. However, the impact of other particles (electrons, ions or neutrals) on the detector can lead to serious deviations. For example, **Figure 5c** shows a very conspicuous region of high intensity in the upper right quadrant. This is the result of either ions or neutrals (produced due to photodetachment or autodetachment) impinging on the detector. The broad, relatively low intensity feature in the spectrum between 0.1 and 0.2 eV is the result of these non-electron impacts. In the current case, the problem could be dealt with mathematically, simply by removing the upper right quadrant data from the analysis. Experimental factors can also be changed in an attempt to remove the spurious signal. Examples include careful manipulation of the timing of the electron imaging pulse (F2), mass discrimination via the timing of the potential switch (E1) or introducing (pulsed) electrostatically charged plates to deflect undesired ions away from the detection region.

Post collection image processing can also affect the velocity (and hence kinetic energy) resolution of the spectra and quantitative analysis of the angular distributions. **Figure 6a** shows the importance of selecting the correct center of the image prior to inverse Abel transformation. The red spectrum is extracted from the F^- image binned to n = 10 and using the best center. The other spectra represent analysis of this binned image using centers with the y coordinate of the specified center increased by 1 (blue), 2 (green) or 3 (orange) pixels. As the chosen center differs more and more from the true image center the spectra broaden, particularly at the base of the transitions and the two peaks begin to coalesce. Additionally, stray external fields (electric and magnetic) and even imperfections in the camera lens lead to distortion of images such that the transitions do not present as perfectly circular features. Integrating over all angles for a particular radius will lead to an apparent broadening of the transition. Examples are shown in **Figure 6b**, c for the F^- image (binned to n = 4) of **Figure 1a**. Comparison of the radial spectrum produced by integrating across two different segments of the angular range (5° degree slices about 36.5° (red) and 86.5° (blue)) is shown in **Figure 6b**. Although the two features in the spectrum are clearly discernible it is also apparent that their maxima are at slightly different radii (302 and 306 for the $^2P_{3/2}$ transition at 36.5° and 86.5° respectively). Further comparison with the radial domain spectrum integrated across the full angular range (**Figure 6b** grey shaded spectrum which is scaled for ease of viewing) shows the effect of the distortion in broadening the spectra. **Figure 6c** (red) shows the eKE domain, fully integrated spectrum of the distorted image. Radial scaling (as a function of angle) before conversion to the energy domain allows correction resulting in the much narrower transitions seen in the fully integrated blue spectrum of **Figure 6c**[42,47]. This is the spectrum originally shown in **Figure 4b** but with the energy scale expanded to better illustrate the effect of an angular dependent radial distortion.

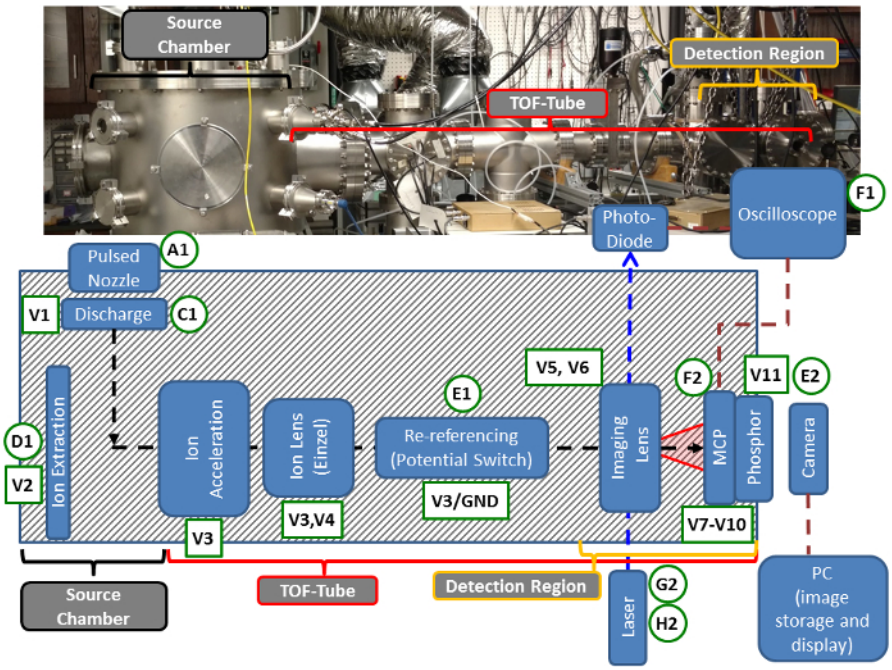

Figure 1. WUSTL anion photoelectron imaging spectrometer. An external view of the vacuum system is displayed at the top. The schematic illustrates the layout of the important components in the experiment. Elements lying within the shaded region are under vacuum. See text for further details. Please click here to view a larger version of this figure.

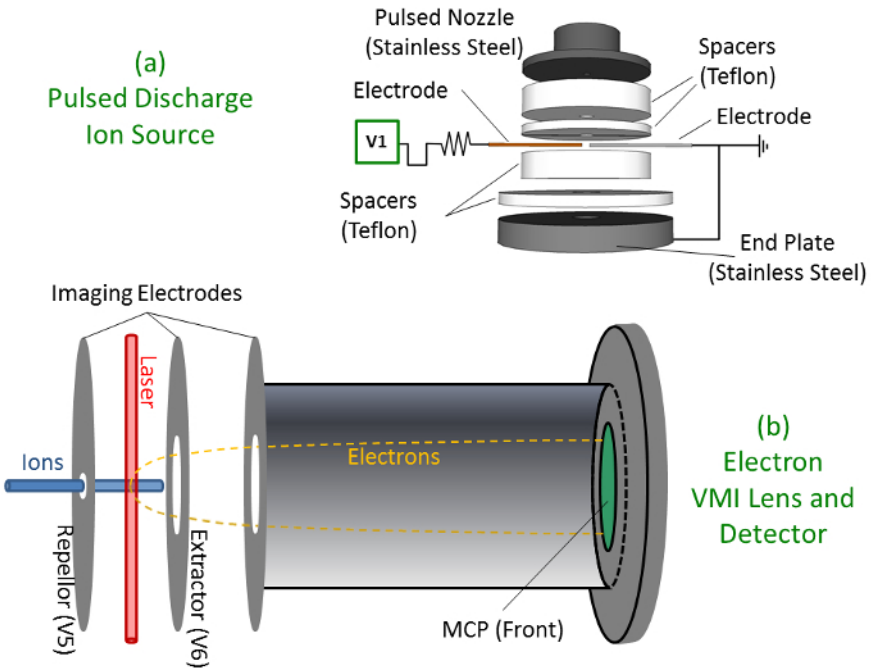

Figure 2. Schematic illustrations of DC discharge and VMI lens assemblies. (a) Anions are produced when a gas pulse travels through the discharge source. **(b)** Electrons produced at the intersection of the ion and laser beams are focused (in momentum space) onto the MCP detector by control of the Extractor and Repeller voltages. Please click here to view a larger version of this figure.

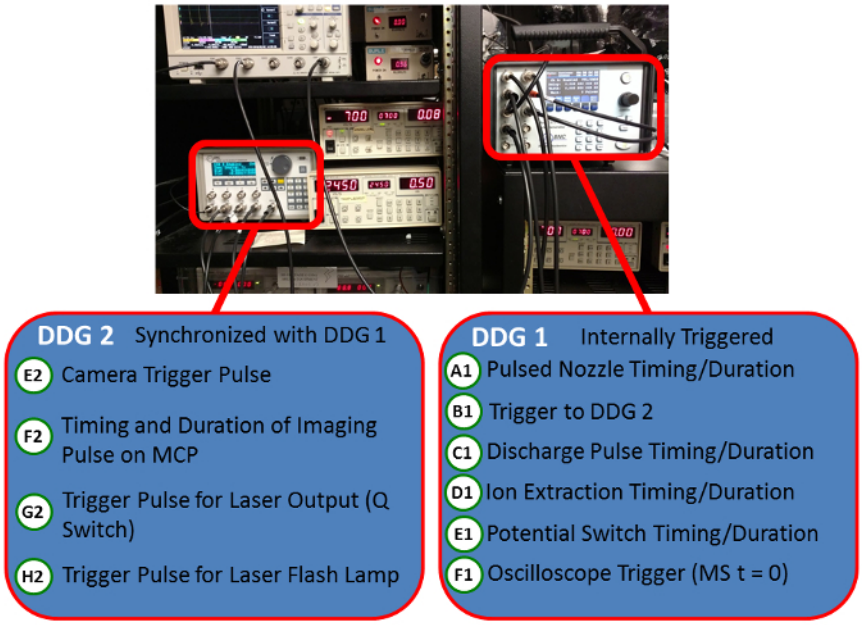

Figure 3. Experiment control. The two digital delay generators (DDG) allow precise control of the experimental timing sequences. Please click here to view a larger version of this figure.

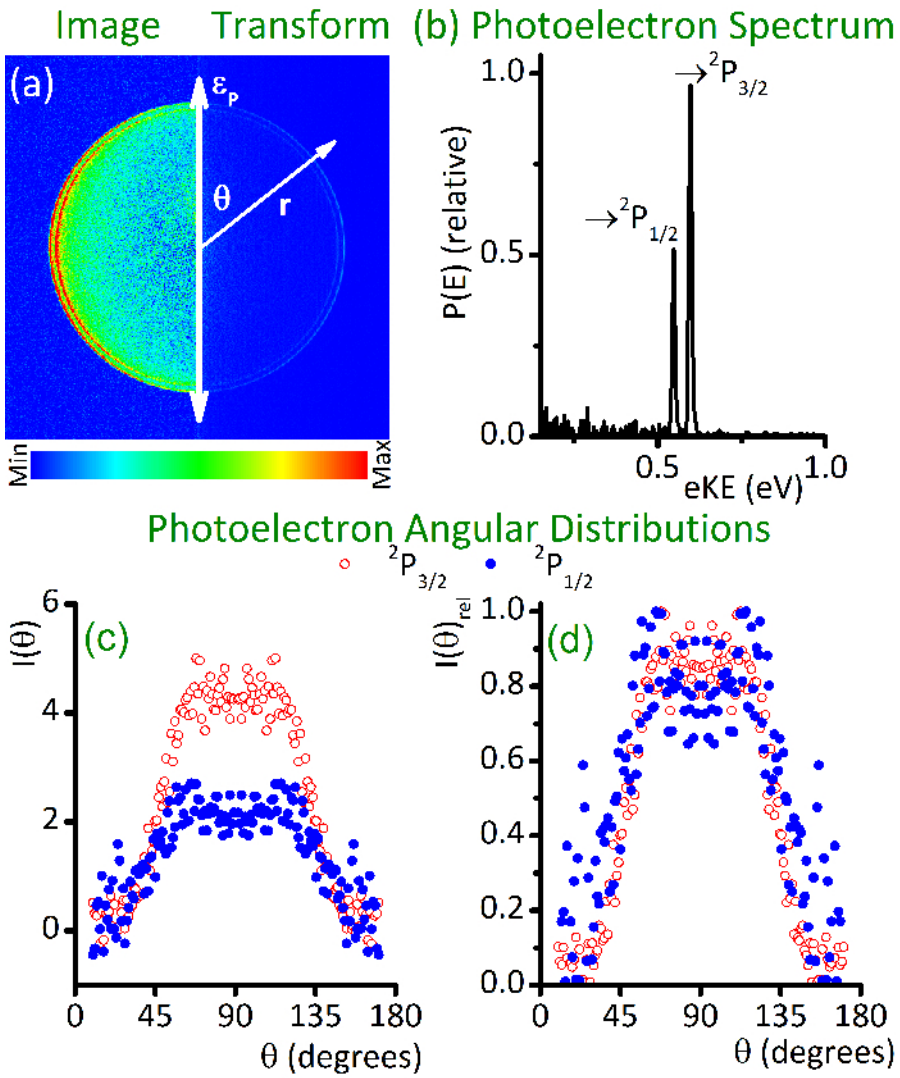

Figure 4. Representative result. (a) Photoelectron image (left half) and inverse Abel transform (right half) for F^- detachment at 4.00 eV. **(b)** The photoelectron spectrum contains two transitions which correspond to the two rings seen in the image. **(c)** The photoelectron angular distributions for each transition in the spectrum (red circles $\rightarrow^2P_{3/2}$, blue circles $\rightarrow^2P_{1/2}$) show the electron distribution in each case is polarized perpendicular to the electric vector of the radiation (ε_p). **(d)** When scaled relative to their respective maxima, the angular distributions for each channel are almost identical. Please click here to view a larger version of this figure.

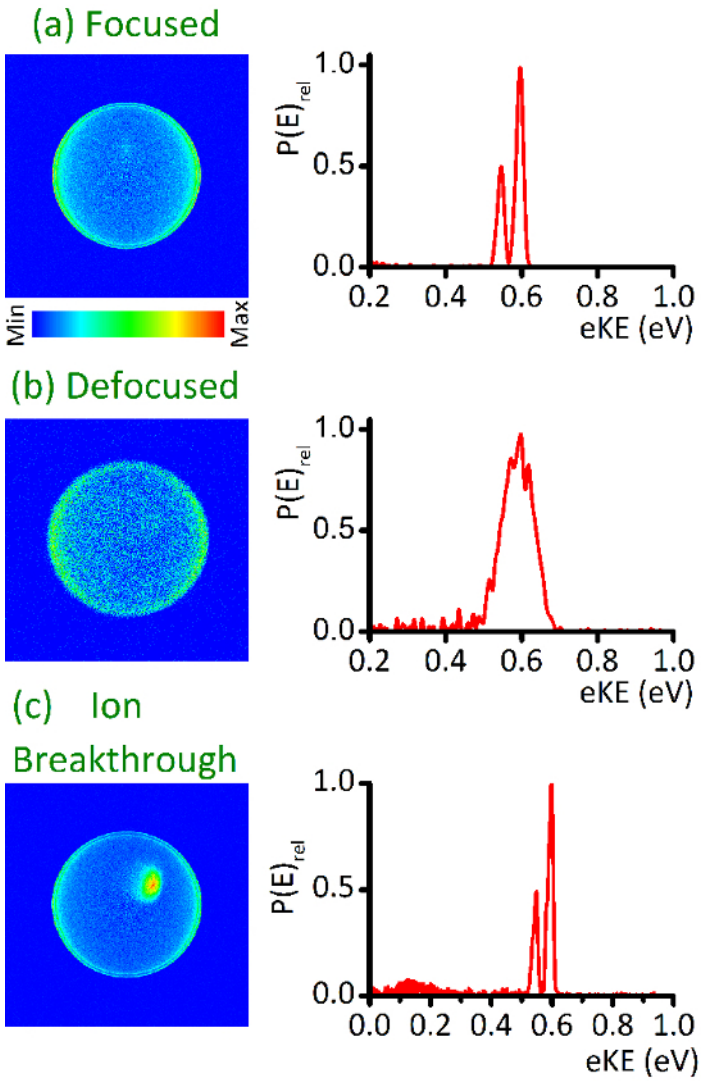

Figure 5. Optimal and less than optimal photoelectron images for F^- detachment at 4.00 eV. The images shown are binned to n = 10. (a) Image at the optimal VMI focusing condition (ratio of 0.700) showing narrow, well resolved peaks in the spectrum. **(b)** Image with a VMI focusing ratio of 0.686 - the two transitions are no longer distinguishable in the spectrum or image. **(c)** The effect of stray ions impinging on the detector coincident with photoelectrons. Please click here to view a larger version of this figure.

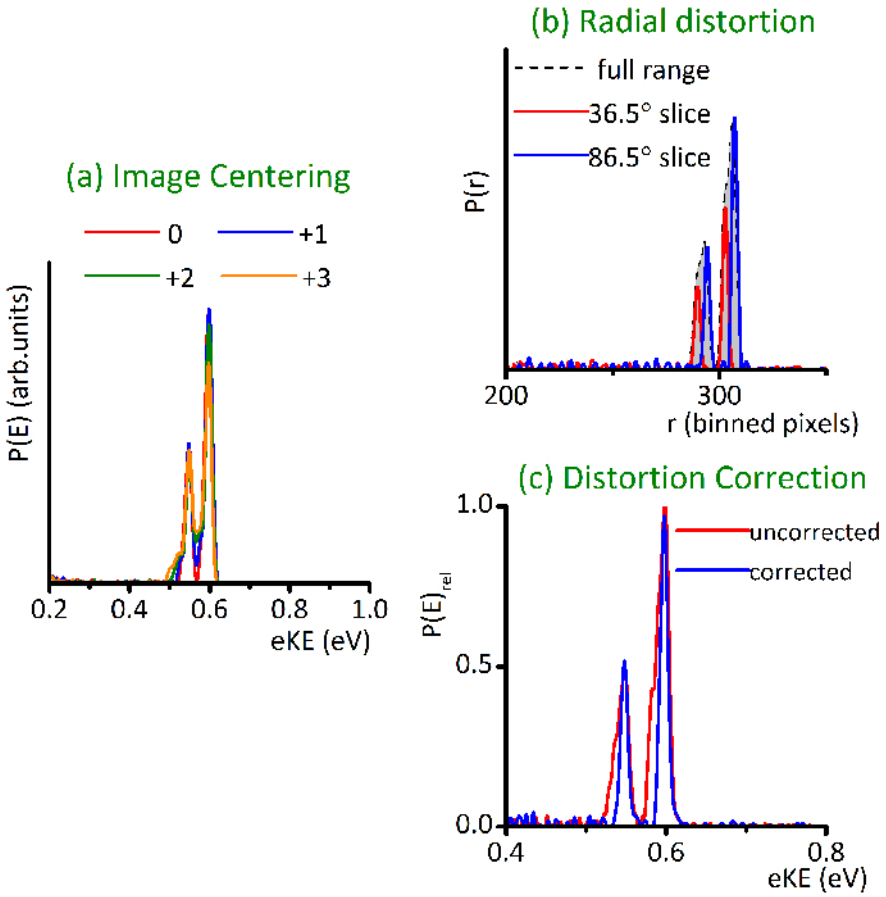

Figure 6. Image analysis/processing effects. (a) Photoelectron spectra are shown extracted from the image of **Figure 4a** with different estimates of the image center. **(b)** Deviation from circularity in the image leads to a loss of resolution. The features in the fully angular integrated spectrum (shaded grey) are considerably broader than those for individual angular segments of the image. **(c)** The effect of the distortion (red spectrum) can be corrected mathematically to recover the full resolution of the detector (blue spectrum). Please click here to view a larger version of this figure.

	Description	Duration (µs)	Delay (µs)	Relative to
A1	Pulsed Nozzle	700	0	DDG1
B1	DDG2 Trigger		0	DDG1
C1	Discharge	70	640	A1
D1	Ion Extraction	7	235	C1
E1	Potential Switch	6	0	D1
F1	Oscilloscope Trigger		0	D1
E2	Camera Trigger		0	B1
F2	Imaging Pulse	1	180.13	H2
G2	Laser Output (Q Switch)		180.94	H2
H2	Laser Trigger (Flash Lamp)		590	B1

Table 1. Experiment pulse timing. The timing of the pulse sequences controlled by the DDGs used in the collection of the image in **Figure 4a**.

	Description		Voltage (kV)
V1	Pulsed Discharge High Voltage		−2.4
V2	Ion Extraction Pulse High Voltage		−1.48
V3	Ion Acceleration Voltage		2.45
	Einzel Lens Outer Elements		
	Potential Switch High Voltage		
V4	Ion Einzel Lens Central Element		1.4
V5	Electron Imaging Lens Repeller		−0.700
V6	Electron Imaging Lens Extractor		−0.497
Ion Mode			
V7	MCP Entry		0.95
V8	MCP Exit		2.51
V9	MCP Power Supply Voltage		3.0
Imaging Mode			
V7	MCP Entry		0.0
V8	MCP Exit		1.0
V9	MCP Power Supply Voltage		1.0
V10	MCP Pulse High Voltage		1.75
V11	Phosphor Screen	Ion Mode	3.2
		Imaging Mode	6.0

Table 2. Applied voltages. Specific voltages applied to the instrument components for the generation of the image in **Figure 4a**.

Discussion

Two factors are particularly critical to the success of the described protocol. The best possible velocity mapping conditions must be determined and more crucially, a sufficient and relatively time invariant yield of the desired anion must be produced. Regarding the VMI focusing steps, steps 5.2 and 5.3 should be repeated in tandem with image analysis to determine the condition which gives the sharpest (narrowest) image features. Fine tuning of the electrode voltages (V5 and V6) is influenced by the size and location of the ion and laser beam intersection, although once the optimum conditions have been achieved for a given system the instrument remains stable. Most important is the ability to produce a particular anion. Paying careful attention to iteratively refining the ion source conditions (inlet gas pressure and composition, discharge electrode materials, vacuum chamber pressure, gas pulse duration, nozzle diameter, discharge pulse voltage, discharge pulse timing and discharge pulse duration) in steps 1-3 is the key. This requires the manipulation of a large number of parameters when initiating the study of a given ion. However, this also allows a large degree of flexibility in the types of ions that can be produced using the discharge source. Application of laser ablation[40], electron impact ionization[19], and entrainment[41] sources along with many other commonly used mass spectrometric techniques is relatively straightforward with only minor instrumental modification. In particular, electrospray methods have been successfully employed to produce higher mass species and doubly charged anions[10,48].

Anion photoelectron spectroscopy is commonly used to probe regions of neutral potential energy surfaces that are inaccessible to techniques such as infra-red absorption spectroscopy. The selection rules for photodetachment are less restrictive, allowing access to a range of neutral vibronic states. Additionally, the inherent charge on the anion allows species selectivity and an electron can typically be removed using commercially available visible/UV light sources. Of the commonly applied photoelectron detection schemes (magnetic bottle spectrometer[49,50], hemispherical analyzer[51,52], photoelectron imaging) the imaging approach confers several advantages. The detection sensitivity is uniform even at very low electron kinetic energies, the imaging technique is inherently efficient (in principle all photoelectrons reach the detector) and imaging simultaneously records the photoelectron angular distribution for each transition in the spectrum in a single measurement. When coupled with a tunable photon source, anion photoelectron imaging also provides an alternative approach to electron scattering experiments in the study of metastable anion states (electron scattering resonances).

The charged particle imaging detection methods in these experiments are essentially limited to the study of species in the gas phase (or at least in vacuo). The MCP detector requires low pressure conditions, the region of interaction between the photons and ions must be as small as possible, the anions require a mean free path greater than the TOF length and the outgoing electrons require a mean free path that significantly exceeds the distance between the interaction region and the detector to preserve the correlation between the detachment event and the detected electron distribution. Nevertheless, studies of cluster anions yield insights of relevance to more condensed phases. For example, the strength of solvation interactions between an anion X^-, and neutral molecules M can be measured by comparison of the X^- and $X^-\cdot M_n$ spectra, where $X^-\cdot M_n$ is a system bound via the ion-molecule interactions.

The experiments use TOF-MS to separate the anions produced in the discharge source. However, situations arise where there are multiple minima on the potential energy surface for a given set of atoms. The mechanism of ion production is highly complex and kinetic trapping can lead to the presence of more than one stable molecular anion isomer, or cluster anion conformer which are not separable by mass in

our instrument. These species usually have different spectral signatures and/or different photoelectron angular distributions which may allow identification and characterization of the isomers/conformers but can also complicate the analysis.

In terms of eKE, photoelectron spectroscopy tends to be a relatively low resolution technique and a disadvantage of imaging is that the energy domain resolution worsens as the eKE increases. In relation to other photoelectron techniques this needs to be weighed against the ability to detect all photoelectrons (compared with the small solid angle collection window of a hemispherical energy analyser)[51,52] with uniform efficiency over all kinetic energies (compared with the decline in efficiency for magnetic bottle spectrometer[49,50] at low kinetic energies). Careful design, control of experimental conditions[32,42], centroiding[43] and distortion correction[42,47] can achieve eKE resolution (ΔeKE/eKE) < 0.5%[32,36,42,53], and absolute resolution of < 1.5 cm^{-1} at very low eKE has been achieved in the closely related SEVI (slow electron velocity mapped imaging) technique[54]. For molecular species the incorporation of cooling ion traps into the ion production stage can also greatly enhance the achieved spectral resolution by narrowing the distribution of populated parent anion internal states[55,56].

One of the most promising applications of VMI in photoelectron spectroscopy is its use in conjunction with a tunable laser source. The photon energy dependence of the spectra and angular distributions can convey information relating to excited anion states. Typically, such states are probed using electron scattering. The photodetachment approach is an alternative allowing good control over the electron energy and crucially the incident electron orbital angular momentum which has the potential to reveal a high degree of detail regarding the electron-neutral interaction. For non-imaging photodetachment, such experiments are extremely time intensive. However, the efficiency of VMI makes such experiments feasible. Application of the approach to O_2^- has shown vibrational dependence of the angular distribution[57,58]. Perhaps more intriguingly, the ability to tune the photon energy allows excitation to and through excited anion states that subsequently lose an electron via autodetachment. These are electron-neutral scattering states. When the photon energy comes into resonance with an internal level (rovibronic) of the excited anion, the absorption probability changes affecting the photoelectron yield. The action spectrum (photoelectron yield as a function of photon energy) reveals details of the internal levels of the excited state. Furthermore, the resolution of the action spectrum is limited by the laser resolution, not the VMI detector. It is therefore possible to (at least partially) resolve rovibronic transitions. This developing application of the technique revealed the location and nature of various excited, metastable states of AgF^- and CuF^-[59,60] (via the angular distributions) and the rotational structure associated with autodetaching vibrational levels of a CH_2CN^- dipole bound state[61]. The information obtained in such experiments is essential to develop understanding of bound and metastable (electron-molecule scattering resonances) negative ion states, doorway states for chemical reduction, dissociative attachment processes and ion-molecule interactions. The results represent vital tests of high level *ab initio* theoretical methods, in particular those which treat highly correlated systems and/or non-stationary states.

Disclosures

The authors have no competing financial interests or other conflicts of interest.

Acknowledgements

This material is based upon work supported by the National Science Foundation under CHE - 1566157

References

1. Sanov, A., Mabbs, R. Photoelectron imaging of negative ions. *International Reviews in Physical Chemistry.* **27** (1), 53-85 (2008).
2. Chandler, D. W., Houston, P. L. Two-dimensional imaging of state-selected photodissociation products detected by multiphoton ionization. *Journal of Chemical Physics.* **87** (2), 1445-1447 (1987).
3. Chandler, D. W., Cline, J. I. Ion imaging applied to the study of chemical dynamics. *Advanced series in physical chemistry.* **14** (1), 61 (2004).
4. Whitaker, B. J. *Imaging in molecular dynamics technology and applications.* Cambridge University Press (2004).
5. Eppink, A. T. J. B., Parker, D. H. Velocity map imaging of ions and electrons using electrostatic lenses - application in photoelectron and photofragment ion imaging of molecular-oxygen. *Review of Scientific Instruments.* **68** (9), 3477-3484 (1997).
6. Davis, A. V., Wester, R., Bragg, A. E., Neumark, D. M. Time resolved photoelectron imaging of the photodissociation of I_2^-. *Journal of Chemical Physics.* **118** (3), 999-1002 (2003).
7. Mabbs, R., Pichugin, K., Surber, E., Sanov, A. Time resolved electron detachment imaging of the I^- channel in I_2Br^- photodissociation. *Journal of Chemical Physics.* **121** (1), 265-271 (2004).
8. Mabbs, R., Pichugin, K., Sanov, A. Time Resolved imaging of the reaction coordinate. *Journal of Chemical Physics.* **122** (17), 174305 (2005).
9. Mabbs, R., Pichugin, K., Sanov, A. Dynamic molecular interferometer: Probe of inversion symmetry in I_2^- photodissociation. *Journal of Chemical Physics.* **123** (5), 054329 (2005).
10. Li, W.-L. *et al.* Photodissociation dynamics of the iodide-uracil (I−U) complex. *Journal of Chemical Physics.* **145** (4), 044319 (2016).
11. King, S. B., Yandell, M. A., Stephansen, A. B., Neumark, D. M. Time-resolved radiation chemistry: Dynamics of electron attachment to uracil following UV excitation of iodide-uracil complexes. *Journal of Chemical Physics.* **141** (22), 224310 (2014).
12. Yandell, M. A., King, S. B., Neumark, D. M. Time-resolved radiation chemistry: Photoelectron imaging of transient negative ions of nucleobases. *Journal of the American Chemical Society.* **135** (6), 2128-2131 (2013).
13. King, S. B., Yandell, M. A., Neumark, D. M. Time-resolved photoelectron imaging of the iodide-thymine and iodide-uracil binary cluster systems. *Faraday Dicsussions.* **163** 59-72 (2013).
14. King, S. B. *et al.* Electron accomodation dynamics in the DNA base thymine. *Journal of Chemical Physics.* **143** (2), 024312 (2015).
15. Stephansen, A. B. *et al.* Dynamics of dipole- and valence bound anions in iodide-adenine binart complexes: A time-resolved photoelectron imaging and quantum mechanical investigation. *Journal of Chemical Physics.* **143** (10), 104308 (2015).
16. Kunin, A., Li, W.-L., Neumark, D. M. Time-resolved photoelectron imaging of iodide-nitromethane ($I^-{\cdot}CH_3NO_2$) photodissociation dynamics. *Physical Chemistry Chemical Physics.* **18** (48), 33226-33232 (2016).
17. Yandell, M. A., King, S. B., Neumark, D. M. Decay dynamics of nascent acetonitrile and nitromethane dipole-bound anions produced by intracluster charge-transfer. *Journal of Chemical Physics.* **140** (18), 184317 (2014).

18. Mabbs, R., Holtgrewe, N., Dao, D., Lasinski, J. Photodetachment and photodissociation of the linear CuO_2^- molecular anion: Energy and time dependence of Cu^- production. *Physical Chemistry Chemical Physics.* **16** (2), 497-504 (2014).
19. Mbaiwa, F., Van Duzor, M., Wei, J., Mabbs, R. Direct and auto-detachment in the iodide-pyrrole cluster anion: The role of dipole bound and neutral cluster states. *Journal of Physical Chemistry A.* **114** (3), 1539-1547 (2010).
20. Osborn, D. L., Leahy, D. J., Cyr, D. M., Neumark, D. M. Photodissociation spectroscopy and dynamics of the $N_2O_2^-$ anion. *Journal of Chemical Physics.* **104** (13), 5026-5039 (1996).
21. Wiley, W. C., McLaren, I. H. Time-of-flight mass spectrometer with improved resolution. *Review of Scientific Instruments.* **26** (12), 1150-1157 (1955).
22. Posey, L. A., DeLuca, M. J., Johnson, M. A. Demonstration of a pulsed photoelectron spectrometer on mass selected negative ions: O^-, O_2^-, AND O_4^-. *Chemical Physics Letters.* **131** (3), 170-174 (1986).
23. Born, M. The statistical interpretation of Quantum Mechanics. *Nobel Lecture.* (1954).
24. Dribinski, V., Ossadtchi, A., Mandelshtam, V. A., Reisler, H. Reconstruction of Abel-transformed images: The Gaussian basis set expansion Abel transform method. *Review of Scientific Instruments.* **73** (7), 2634-2642 (2002).
25. Hansen, E. W., Law, P.-L. Recursive methods for computing the Abel transform and its inverse. *Journal of the Optical Society of America A.* **2** (4), 510-519 (1985).
26. Dasch, C. J. One-dimensional tomography: a comparison of Abel, onion-peeling, and filtered backprojection methods. *Applied Optics.* **31** (8), 1146-1152 (1992).
27. Manzhos, S., Loock, H.-P. Photofragment image analysis using the Onion-Peeling algorithm. *Computer Physics Communications.* **154** (1), 76-87 (2003).
28. Van Duzor, M., Mbaiwa, F., Wei, J., Mabbs, R. The effect of intra-cluster photoelectron interactions on the angular distribution in $I^-{\cdot}CH_3I$ photodetachment. *Journal of Chemical Physics.* **131** (20), 204306 (2009).
29. Surber, E., Ananthavel, S. P., Sanov, A. Nonexistent electron affinity of OCS and the stabilization of carbonyl sulfide anions by gas phase hydration. *Journal of Chemical Physics.* **116** (5), 1920-1929 (2002).
30. Velarde, L., Habteyes, T., Sanov, A. Photodetachment and photofragmentation pathwaysin the $[(CO_2)_2(H_2O)_m]^-$ cluster anions. *Journal of Chemical Physics.* **125** (11), 114303 (2006).
31. Rathbone, G. J., Sanford, T., Andrews, D., Lineberger, W. C. Photoelectron imaging spectroscopy of $Cu^-(H_2O)_{1,2}$ anion complexes. *Chemical Physics Letters.* **401** (4-6), 570-574 (2005).
32. Leon, I., Yang, Z., Liu, H.-T., Wang, L.-S. The design and construction of a high-resolution velocity-map imaging apparatus for photoelectron spectroscopy studies of size-selected clusters. *Review of Scientific Instruments.* **85** (8), 083106 (2014).
33. Silva, W. R., Cao, W., Yang, D.-S. Low-energy photoelectron imaging spectrsocopy of La_n(benzene) (n = 1 and 2). *Journal of Physical Chemistry A.* **121** (44), 8440-8447 (2017).
34. Mann, J. E., Troyer, M. E., Jarrold, C. C. Photoelectron imaging and photodissociation of ozonide in $O_3^-{\cdot}(O_2)_n$ (n = 1-4) clusters. *Journal of Chemical Physics.* **142** (12), 124305 (2015).
35. Horke, D. A., Roberts, G. M., Lecointre, J., Verlet, J. R. R. Velocity-map imaging at low extraction fields. *Review of Scientific Instruments.* **83** (6), 063101 (2012).
36. Osterwalder, A., Nee, M. J., Zhou, J., Neumark, D. M. High resolution photodetachment spectroscopy of negative ions via slow photoelectron imaging. *Journal of Chemical Physics.* **121** (13), 6317-6322 (2004).
37. Liu, Q.-Y. *et al.* Photoelectron imaging spectrsocopy of MoC^- and NbN^- diatomic anions: a comparitive study. *Journal of Chemical Physics.* **142** (16), 164301 (2015).
38. Sobhy, M. A., Castleman, A. W. Photoelectron imaging of copper and silver mono- and diamine anions. *Journal of Chemical Physics.* **126** (15), 154314 (2007).
39. Qin, Z., Wu, X., Tang, Z. Note: A novel dual-channel time-of-flight mass spectrometer for photoelectron imaging spectroscopy. *Review of Scientific Instruments.* **84** (6), 066108 (2013).
40. Xie, H. *et al.* Probing the structural and electronic properties of Ag_nH^- (n = 1-3) using photoelectron imaging and theoretical calculations. *Journal of Chemical Physics.* **136** (18), 184312 (2012).
41. Adams, C. L., Schneider, H., Ervin, K. M., Weber, J. M. Low-energy photoelectron imaging spectroscopy of nitromethane anions: Electron affinity, vibrational features, anisotropies, and the dipole-bound state. *Journal of Chemical Physics.* **130** (7), 074307 (2009).
42. Cavanagh, S. J. *et al.* High-Resolution velocity map imaging photoelectron spectroscopy of the O^- photodetachment fine-structure transitions. *Physical Review A.* **76** (5), 052708 (2007).
43. Li, W., Chambreau, S. D., Lahankar, S. A., Suits, A. G. Megapixel imaging with standard video. *Review of Scientific Instruments.* **76** (6), 063106 (2005).
44. Blondel, C., Delsart, C., Goldfarb, F. Electron spectrometry at the μeV level and the electron affinities of Si and F. *Journal of Physics B.* **34** (9), L281-288 (2001).
45. Mabbs, R., Grumbling, E. R., Pichugin, K., Sanov, A. Photoelectron imaging: An experimental window into electronic structure. *Chemical Society Reviews.* **38** (8), 2169-2177 (2009).
46. Grumbling, E. R., Pichugin, K., Mabbs, R., Sanov, A. Photoelectron imaging as a quantum chemistry visualization tool. *Journal of Chemical Education.* **88** (11), 1515-1520 (2011).
47. Gascooke, J. R., Gibson, S. T., Lawrance, W. D. A "circularisation" method to repair deformations and determine the centre of velocity map images. *Journal of Chemical Physic.* **147** (1), 013924 (2017).
48. Xing, X.-P., Wang, X.-B., Wang, L.-S. Photoelectron angular distribution and molecular structure in multiply charged anions. *Journal of Physical Chemistry A.* **113** (6), 945-948 (2008).
49. Tsuboi, T., Xu, E. Y., Bae, Y. K., Gillen, K. T. Magnetic bottle electron spectrometer using permanent magnets. *Review of Scientific Instruments.* **59** (6), 1357-1362 (1988).
50. Kruit, P., Read, F. H. Magnetic field paralleliser for 2π electron-spectrometer and electron image magnifier. *Journal of Physics E.* **16** (4), 313-324 (1983).
51. Travers, M. J., Cowles, D. C., Clifford, E. P., Ellison, G. B., Engelking, P. C. Photoelectron spectroscopy of the CH_3N^- ion. *Journal of Chemical Physics.* **111** (12), 5349-5360 (1999).
52. Ellis Jr., H. B., Ellison, G. B. Photoelectron spectroscopy of HNO^- and DNO^-. *Journal of Chemical Physics.* **78** (11), 6541-6558 (1983).
53. Cavanagh, S. J., Gibson, S. T., Lewis, B. R. High-resolution photoelectron spectroscopy of linear← bent polyatomic photodetachment transitions: The electron affinity of CS_2. *Journal of Chemical Physics.* **137** (14), 144304 (2012).

54. Neumark, D. M. Slow electron velocity-map imaging of negative Ions: Applications to spectroscopy and dynamics. *The Journal of Physical Chemistry A.* **112** (51), 13287-13301 (2008).
55. Weichman, M. L., Kim, J. B., Neumark, D. M. Rovibronic structure in slow photoelectron velocity-map imaging spectroscopy of CH_2CN^- and CD_2CN^-. *Journal of Chemical Physics.* **140** (10), 104305 (2014).
56. Huang, D.-L., Zhu, G.-Z., Liu, Y., Wang, L.-S. Photodetachment spectroscopy and resonant photoelectron imaging of cryogenically-cooled deprotonated 2-hydroxypyrimidine anions. *Journal of Molecular Spectroscopy.* **332** 86-93 (2017).
57. Van Duzor, M. *et al.* Vibronic coupling in the superoxide anion: The vibrational dependence of the photoelectron angular distribution. *Journal of Chemical Physics.* **133** (17), 174311 (2010).
58. Mabbs, R. *et al.* Observation of vibration-dependent electron anisotropy in O_2^- photodetachment. *Physical Review A.* **82** (1), 011401(R) (2010).
59. Dao, D. B., Mabbs, R. The effect of the dipole bound state on AgF^- vibrationally resolved photodetachment cross sections and photoelectron angular distributions. *Journal of Chemical Physics.* **141** (15), 154304 (2014).
60. Jagau, T. C., Dao, D. B., Holtgrewe, N., Krylov, A. I., Mabbs, R. Same but Different: Dipole-Stabilized Shape Resonances in CuF^- and AgF^-. *Journal of Physical Chemistry Letters.* **6** (14), 2786-2793 (2015).
61. Lyle, J., Wedig, O., Gulania, S., Krylov, A. I., Mabbs, R. Channel branching ratios in CH_2CN^-photodetachment: Rotational structure and vibrational energy redistribution in autodetachment. *Journal of Chemical Physics.* **147** (23), 234309 (2017).

